

Discovery of gamma-ray halos around active galactic nuclei and the first measurement of intergalactic magnetic fields

Shin'ichiro Ando¹ & Alexander Kusenko^{2,3}

¹California Institute of Technology, Mail Code 350-17, Pasadena, CA 91125, USA

²Department of Physics & Astronomy, University of California, Los Angeles, CA 90095, USA

³Institute for the Physics & Mathematics of the Universe, University of Tokyo, Kashiwa, Chiba 277-8568, Japan

Magnetic fields in intergalactic space had not been measured until now, despite their importance for gamma-ray and cosmic-ray astronomy and their likely connection to the primordial fields that could have seeded the stronger magnetic fields observed in galaxies, Sun, and Earth¹⁻⁴. It has long been expected that intergalactic magnetic fields (IGMF) should cause the appearance of halos around the gamma-ray images of distant objects because an electromagnetic cascade initiated by a high-energy gamma-ray interaction with the photon background is broadened by the magnetic deflections⁵. Here we report the discovery of gamma-ray halos in the stacked images of 170 brightest active galactic nuclei (AGN) in the 11-month source catalog of the *Fermi* Gamma-Ray Space Telescope⁶. The dependence of the halo size and brightness on the gamma-ray energy and the source distance is consistent with IGMF, $B \approx 10^{-15} \text{ G} (\lambda_B/1 \text{ kpc})^{-1/2}$ and $\lambda_B < 10\text{--}100 \text{ kpc}$, where B and λ_B are the strength and correlation length of IGMF, respectively. The knowledge of IGMF will facilitate the future gamma-ray and charged-particle astronomy. Furthermore, since IGMF are likely to originate from the primordial seed fields created shortly after the Big Bang, this discovery opens a new window on the origin of cosmological magnetic fields⁷, inflation^{8,9}, and the phase transitions^{10,11} in the early universe.

IGMF are too small to be measured by conventional astronomical probes, such as Zeeman splitting or Faraday rotation. Unlike the fields in galaxies, which are believed to have been amplified by the dynamo action associated with the large-scale convective motions of gas, the fields in the voids remain low, close to their primordial values modified only by the relatively small contribution of the fields leaking out of galaxies. The observational and theoretical upper bounds on IGMF constrain their magnitudes to be below 10^{-9} G ¹², whereas any value above $\sim 10^{-30} \text{ G}$ is sufficient to explain the $\sim \mu\text{G}$ galactic magnetic fields generation by the dynamo mechanism¹³.

One can detect such extremely weak fields using high-energy gamma rays^{5,14}. Very energetic photons emitted from AGN or another strong source produce pairs of electrons and positrons in their interactions with extragalactic background light (EBL). These pairs up-scatter the cosmic microwave background photons to high energies, giving rise to an electromagnetic cascade, and the photons from the cascade are detected by gamma-ray telescopes, such as *Fermi*. Since the

trajectories of electrons and positrons in the cascade are affected by magnetic fields, the gamma-ray images of AGN are expected to exhibit a halo of secondary photons around a bright central point-like source^{5,15,16}. The central image is expected to be composed of photons emitted directly from the source with energies below the pair production threshold. In addition, delays in arrival times of the secondary photons can be used to probe IGMF^{14,17,18}. Finally, at TeV energies, the secondary photons produced in interactions of cosmic rays with the photon background may have already been observed by the air Cherenkov telescopes^{19,20}.

Thus far, in TeV range, HEGRA²¹ and MAGIC²² did not detect any halo component of two bright blazars, Mrk 501 and Mrk 421, and they set upper limits on the flux. In particular, the analysis of MAGIC using gamma rays above 300 GeV excludes some regions of IGMF between 4×10^{-15} and 10^{-14} G. Very recently, IGMF above 3×10^{-16} G were proposed as an explanation of non-observation by *Fermi* of several AGN known to be bright TeV sources²³.

Here we present the discovery of extended images and of IGMF using gamma-ray data collected by the Large Area Telescope (LAT) onboard *Fermi*, in the energy range between 1 GeV and 100 GeV. The individual photon data as well as the 11-month source catalog²⁴ are now publicly available at <http://fermi.gsfc.nasa.gov/ssc/>. Among ~ 700 AGN in the Fermi AGN catalog⁶, we select 170 AGN that are detected at more than 4σ in the highest energy band, 10–100 GeV, and located at high Galactic latitudes, $|b| > 10^\circ$. These sources are likely to have a hard spectrum, and produce a large number of TeV primary photons, which is necessary for the appearance of the secondary halo. Although each individual AGN produces too few photon counts, especially in the highest-energy band, one can dramatically improve the statistics by stacking all these 170 AGN maps. We perform the analysis in three separate energy bands: 1–3 GeV, 3–10 GeV, and 10–100 GeV, which allows us to study the energy dependence of the halos. To obtain source and model maps, we use official *Science Tools* made publicly available by the *Fermi* team.

Figure 1 shows the gamma-ray count maps of stacked 170 AGN and the “best-fit” point-source model generated with the *Fermi Science Tools* as well as point-source catalog, smeared only by point spread function (PSF) of LAT (we use “Pass6 version 3” instrument response function of LAT). It is evident that the counts map and the model map are not consistent with each other, especially in the 10–100 GeV range. (We do not show the 1–3 GeV maps here, because there is no apparent visual difference between the counts and model maps.)

We have performed maximum likelihood analysis assuming that, in addition to the central point sources and diffuse (Galactic^{25,26} and extragalactic²⁷) backgrounds, there is a third component, namely, the halo component, whose spatial extent is given by the Gaussian distribution:

$$P_{\text{halo}}(\theta^2|\theta_{\text{halo}}^2) = \frac{2}{\pi\theta_{\text{halo}}^2} \exp\left(-\frac{\theta^4}{\pi\theta_{\text{halo}}^4}\right), \quad (1)$$

where θ is the angle from the map center, and θ_{halo}^2 is the mean of θ^2 over this distribution function, $\theta_{\text{halo}}^2 \equiv \langle \theta^2 \rangle$. We fit the histogram of photon counts as a function of θ^2 read from the maps by

minimizing

$$\chi^2 = \sum_i \frac{1}{N_i} [N_{\text{psf}} P_{\text{psf}}(\theta_i^2) + N_{\text{halo}} P_{\text{halo}}(\theta_i^2 | \theta_{\text{halo}}^2) + N_{\text{bg},i} - N_i]^2, \quad (2)$$

where N_{psf} , N_{halo} , and θ_{halo} are treated as free parameters. The index i refers to the i -th bin, N_i is the total number of events in this bin, P_{psf} is the normalized PSF, and $N_{\text{bg},i}$ is the events due to diffuse background, for which we fix values at large θ^2 assuming that the background is homogeneous. (This is a very good approximation because we average the background map over many AGN images.) Thus, N_{psf} and N_{halo} are the total numbers of photons in the map attributed to the point source and the halo, respectively, and θ_{halo} is the apparent angular extent of the halo component.

The inclusion of the halo component improves the fit significantly at high energies, but not in the lowest 1–3 GeV band. The minimum χ^2 over degree of freedom (ν) is $\chi_{\text{min}}^2/\nu = 18.8/19$ and $13.3/12$ for 3–10 GeV and 10–100 GeV, respectively. In contrast, the “best-fit” point-source model gives $\chi^2 \simeq 69$ and 140 for 3–10 GeV and 10–100 GeV, respectively. This clearly shows that, even though we stack many AGN, this simple Gaussian halo model gives a very good fit to the data. The surface brightness profiles $dN/d\theta^2$ of the best-fit halo model are juxtaposed with the data points in Fig. 2.

In the upper panel of Fig. 3, we show the allowed regions of θ_{halo} and f_{halo} at 68% and 95% confidence levels. Here f_{halo} is the fraction of the halo photons, i.e., $f_{\text{halo}} \equiv N_{\text{halo}}/(N_{\text{psf}} + N_{\text{halo}})$. The best-fit values and 1σ errors for these parameters are $\theta_{\text{halo}} = 0.49 \pm 0.06$ deg and $f_{\text{halo}} = 0.097_{-0.026}^{+0.025}$ for 3–10 GeV, and $\theta_{\text{halo}} = 0.26_{-0.02}^{+0.03}$ deg and $f_{\text{halo}} = 0.20_{-0.04}^{+0.03}$ for 10–100 GeV. For the lowest energy band, 1–3 GeV, only an upper limit on f_{halo} is obtained, which is $f_{\text{halo}} < 0.057$ at 95% confidence level.

We interpret the size of the halo θ_{halo} shown in the top panel of Fig. 3, in terms of the secondary photon model, especially parameters of IGMF. A simple analytic model gives the following relation between these quantities¹⁶:

$$\theta_{\text{halo}} = \begin{cases} 5^\circ (1+z)^{-2} \tau^{-1} \left(\frac{E_\gamma}{10 \text{ GeV}} \right)^{-1} \left(\frac{B}{10^{-15} \text{ G}} \right), & \text{for } \lambda_B \gg D_e, \\ 0.4^\circ (1+z)^{-1/2} \tau^{-1} \left(\frac{E_\gamma}{10 \text{ GeV}} \right)^{-3/4} \left(\frac{B}{10^{-15} \text{ G}} \right) \left(\frac{\lambda_B}{1 \text{ kpc}} \right)^{1/2}, & \text{for } \lambda_B \ll D_e, \end{cases} \quad (3)$$

where E_γ is the gamma-ray energy, z is the redshift of the source, τ is the optical depth for the TeV photons that produce halo gamma rays, and D_e is the energy-loss length of the electrons and positrons produced by primary TeV photons. Because the lower-energy secondary photons originate from the less energetic electrons and positrons that are deflected by larger angles in IGMF, one expects a larger halo size θ_{halo} at lower energy, which explains qualitatively the energy dependence in Eq. (3). As for the dependence on the correlation length of IGMF, λ_B , if λ_B is much longer than D_e , then the charged particles can be regarded as propagating in a homogeneous magnetic fields (equivalent to infinite λ_B), and, therefore, the deflection angle is given by the ratio of D_e and the Larmor radius. If λ_B is much smaller than D_e , on the other hand, then the electrons and positrons

propagate by random walk, with deflections proportional to $\lambda_B^{1/2}$. The energy dependence of θ_{halo} shown in Fig. 3 implies that the data prefer the case of small correlation length ($\lambda_B < 0.01\text{--}0.1$ Mpc), but we cannot exclude the opposite case completely, because approximations made to obtain Eq. (3) may not hold at low-energy regime such as $E_\gamma \sim 1$ GeV¹⁶. Assuming $\tau \sim 1$ and using an average redshift of the stacked AGN (99 out of 170 have measured redshifts), $\langle z \rangle \sim 0.6$, we obtain $B \approx 10^{-15} \text{ G} (\lambda_B/1 \text{ kpc})^{-1/2}$ for $\lambda_B < 0.01\text{--}0.1$ Mpc. This is the first measurement of the strength and correlation length of IGMF based on a positive detection.

The energy dependence of halo fraction f_{halo} is also consistent with our interpretation. Based on the average spectral index in our sample of AGN, $\langle p \rangle = 1.98$, we assume that the primary photon spectrum follows single power law $dF_\gamma/dE_\gamma \propto E_\gamma^{-2}$. Assuming that the LAT exposure is independent of energy, the number of detected primary photons scales as $N_{\text{psf}} \propto E_{\text{min}}^{-1} - E_{\text{max}}^{-1} \sim E_{\text{min}}^{-1}$, where E_{min} and E_{max} are the minimum and maximum energies of a given band. The flux of the secondary photons, on the other hand, depends on the total energy (not the total number) of TeV photons that produce cascades. Hence, the flux of the halo component scales as $N_{\text{halo}} \propto \ln(E_{\text{max}}/E_{\text{min}})$. The ratio is, therefore, $f_{\text{halo}} \sim N_{\text{halo}}/N_{\text{psf}} \sim E_{\text{min}} \ln(E_{\text{max}}/E_{\text{min}})$, which qualitatively explains the tendency seen in Fig. 3, as well as the absence of significant halos in the 1–3 GeV band.

At the mean redshift of the sample ($\langle z \rangle = 0.6$), the observed halo size of $\sim 0.2\text{--}0.6^\circ$ corresponds to 5–15 Mpc. There are no known astrophysical sources capable of producing images of such a large size. Therefore, we conclude that the halos of the secondary photons provide the only realistic explanation of the data.

Finally, we discuss the possibility that these halos could be due to some unknown instrumental effect, such as, for example, a possible deviation of LAT PSF from its value measured in calibration prior to the launch. To exclude such a possibility, we consider samples of AGN at different redshifts, because any instrumental effect should be redshift independent. We divide the 99 AGN with known distances (out of total 170) into two groups: a sample of 57 nearby AGN with $z < 0.5$ ($\langle z \rangle \approx 0.2$), and a sample of 42 distant AGN with $0.5 < z < 2.5$ ($\langle z \rangle \approx 0.8$). The allowed regions of θ_{halo} and f_{halo} for these two samples, both for 3–10 GeV and 10–100 GeV, are shown in the bottom panel of Fig. 3. The statistically significant difference between the two populations shown in this figure implies that the halos cannot be attributed to an instrumental effect.

At the same time, the redshift behaviors of both θ_{halo} and f_{halo} shown in Fig. 3 are consistent with the effects of IGMF. Based on Eq. (3), in the case of small λ_B , θ_{halo} is expected to be a slowly varying function of redshift, $\theta_{\text{halo}} \propto (1+z)^{-1/2}$. A weak dependence of θ_{halo} on the redshift is evident for the 10–100 GeV sample, and it is not inconsistent with the results for the 3–10 GeV sample, where the large spread in θ_{halo} prevents one from drawing a conclusion.

To understand the redshift dependence of f_{halo} , we observe that, in the limit of small angles, the halo flux is proportional to the square of the angular size δ of the electromagnetic cascade.

The latter depends on the primary photon energy¹⁶ as $\delta \propto E^{-3/2}$. Therefore, the photons of the lowest energy, but still energetic enough to pair-produce off EBL, make the dominant contribution to f_{halo} . For each redshift z , this requirement defines an optimal energy $E_{\text{opt}}(z)$, for which the optical depth is $\tau \sim 1$. One can show that $E_{\text{opt}} \propto (1+z)^{-\alpha}$, where $2 < \alpha < 3$. For a power-law spectrum $dN/dE \propto E^{-p}$, the total energy carried by such photons is $\propto E_{\text{opt}}^{-p+2}$, and therefore, $f_{\text{halo}} \propto (1+z)^{-\alpha(2-p)}$. In our sample, p is close to 2, with a trend $p > 2$ at high energies and $p < 2$ at low energies. Thus, both the decrease of f_{halo} with the redshift in the 3–10 GeV range and the absence of such a decrease at high energy are consistent with the effects of IGMF.

As yet another independent test to rule out instrumental effects, we considered a sample of 42 AGN from the same catalog²⁴, which produced no photons above 10 GeV, but which were detected in the 3–10 GeV band at more than 4σ . These sources are likely to have a softer spectrum, with a negligible flux of primary photons above the pair production threshold. In the absence of pair production, one expects to see no halos. As expected, the best fit in the 3–10 GeV energy band is achieved for $f_{\text{halo}} = 0$, with an upper limit of $f_{\text{halo}} < 0.1$ at 95% confidence level.

Based on several independent but consistent tests, we conclude that the halos cannot be attributed to instrumental effects.

In summary, we have reported a discovery of gamma-ray halos around the AGN images obtained by *Fermi*. These halos are not caused by extended sources or instrumental effects. They are consistent with IGMF $B \approx 10^{-15}$ G $(\lambda_B/1 \text{ kpc})^{-1/2}$. Moreover, the data strongly favor $\lambda_B < 10$ –100 kpc.

1. Kronberg, P. P. Extragalactic magnetic fields. *Rept. Prog. Phys.* **57**, 325–382 (1994).
2. Grasso, D. & Rubinstein, H. R. Magnetic fields in the early universe. *Phys. Rept.* **348**, 163–266 (2001).
3. Widrow, L. M. Origin of Galactic and Extragalactic Magnetic Fields. *Rev. Mod. Phys.* **74**, 775–823 (2002).
4. Kulsrud, R. M. & Zweibel, E. G. The Origin of Astrophysical Magnetic Fields. *Rept. Prog. Phys.* **71**, 0046091 (2008).
5. Aharonian, F. A., Coppi, P. S. & Volk, H. J. Very high-energy gamma-rays from AGN: Cascading on the cosmic background radiation fields and the formation of pair halos. *Astrophys. J.* **423**, L5–L8 (1994).
6. Abdo, A. A. *et al.* The First Catalog of Active Galactic Nuclei Detected by the Fermi Large Area Telescope. *Astrophys. J.* **715**, 429–457 (2010).
7. Cornwall, J. M. Speculations on primordial magnetic helicity. *Phys. Rev. D* **56**, 6146–6154 (1997).

8. Turner, M. S. & Widrow, L. M. Inflation Produced, Large Scale Magnetic Fields. *Phys. Rev. D* **37**, 2743 (1988).
9. Diaz-Gil, A., Garcia-Bellido, J., Garcia Perez, M. & Gonzalez-Arroyo, A. Magnetic field production during preheating at the electroweak scale. *Phys. Rev. Lett.* **100**, 241301 (2008).
10. Vachaspati, T. Magnetic fields from cosmological phase transitions. *Phys. Lett. B* **265**, 258–261 (1991).
11. Baym, G., Bodeker, D. & McLerran, L. D. Magnetic fields produced by phase transition bubbles in the electroweak phase transition. *Phys. Rev. D* **53**, 662–667 (1996).
12. Barrow, J. D., Ferreira, P. G. & Silk, J. Constraints on a Primordial Magnetic Field. *Phys. Rev. Lett.* **78**, 3610–3613 (1997).
13. Davis, A., Lilley, M. & Törnkvist, O. Relaxing the bounds on primordial magnetic seed fields. *Phys. Rev. D* **60**, 021301 (1999).
14. Plaga, R. Detecting intergalactic magnetic fields using time delays in pulses of γ -rays. *Nature* **374**, 430–432 (1995).
15. Dolag, K., Kachelriess, M., Ostapchenko, S. & Tomas, R. Blazar halos as probe for extragalactic magnetic fields and maximal acceleration energy. *Astrophys. J.* **703**, 1078–1085 (2009).
16. Neronov, A. & Semikoz, D. V. Sensitivity of gamma-ray telescopes for detection of magnetic fields in intergalactic medium. *Phys. Rev. D* **80**, 123012 (2009).
17. Ando, S. Does regenerated emission change the high-energy signal from gamma-ray burst afterglows? *Mon. Not. Roy. Astron. Soc.* **354**, 414–418 (2004).
18. Murase, K., Takahashi, K., Inoue, S., Ichiki, K. & Nagataki, S. Probing Intergalactic Magnetic Fields in the GLAST Era through Pair Echo Emission from TeV Blazars. *Astrophys. J.* **686**, L67–L70 (2008).
19. Essey, W. & Kusenko, A. A new interpretation of the gamma-ray observations of distant active galactic nuclei. *Astropart. Phys.* **33**, 81–85 (2010).
20. Essey, W., Kalashev, O. E., Kusenko, A. & Beacom, J. F. Secondary Photons and Neutrinos from Cosmic Rays Produced by Distant Blazars. *Phys. Rev. Lett.* **104**, 141102 (2010).
21. Aharonian, F. A. *et al.* Search for a TeV gamma-ray halo of Mkn 501. *Astron. Astrophys.* **366**, 746–751 (2001).
22. Aleksic, J. *et al.* Search for an extended VHE gamma-ray emission from Mrk 421 and Mrk 501 with the MAGIC Telescope (2010). 1004.1093.

23. Neronov, A. & Vovk, I. Evidence for strong extragalactic magnetic fields from Fermi observations of TeV blazars. *Science* **328**, 73–75 (2010).
24. Abdo, A. A. *et al.* Fermi Large Area Telescope First Source Catalog (2010). 1002.2280.
25. Abdo, A. A. *et al.* Fermi Large Area Telescope Measurements of the Diffuse Gamma-Ray Emission at Intermediate Galactic Latitudes. *Phys. Rev. Lett.* **103**, 251101 (2009).
26. Strong, A. W., Moskalenko, I. V. & Reimer, O. Diffuse Galactic continuum gamma rays. A model compatible with EGRET data and cosmic-ray measurements. *Astrophys. J.* **613**, 962–976 (2004).
27. Abdo, A. A. *et al.* The Spectrum of the Isotropic Diffuse Gamma-Ray Emission Derived From First-Year Fermi Large Area Telescope Data. *Phys. Rev. Lett.* **104**, 101101 (2010).

Acknowledgements The work of S.A. was supported by Japan Society for Promotion of Science and partially by NASA through the Fermi GI Program grant NNX09AT74G. The work of A.K. was supported by DOE grant DE-FG03-91ER40662 and NASA ATFP grant NNX08AL48G.

Correspondence Correspondence should be addressed to S.A. (ando@caltech.edu).

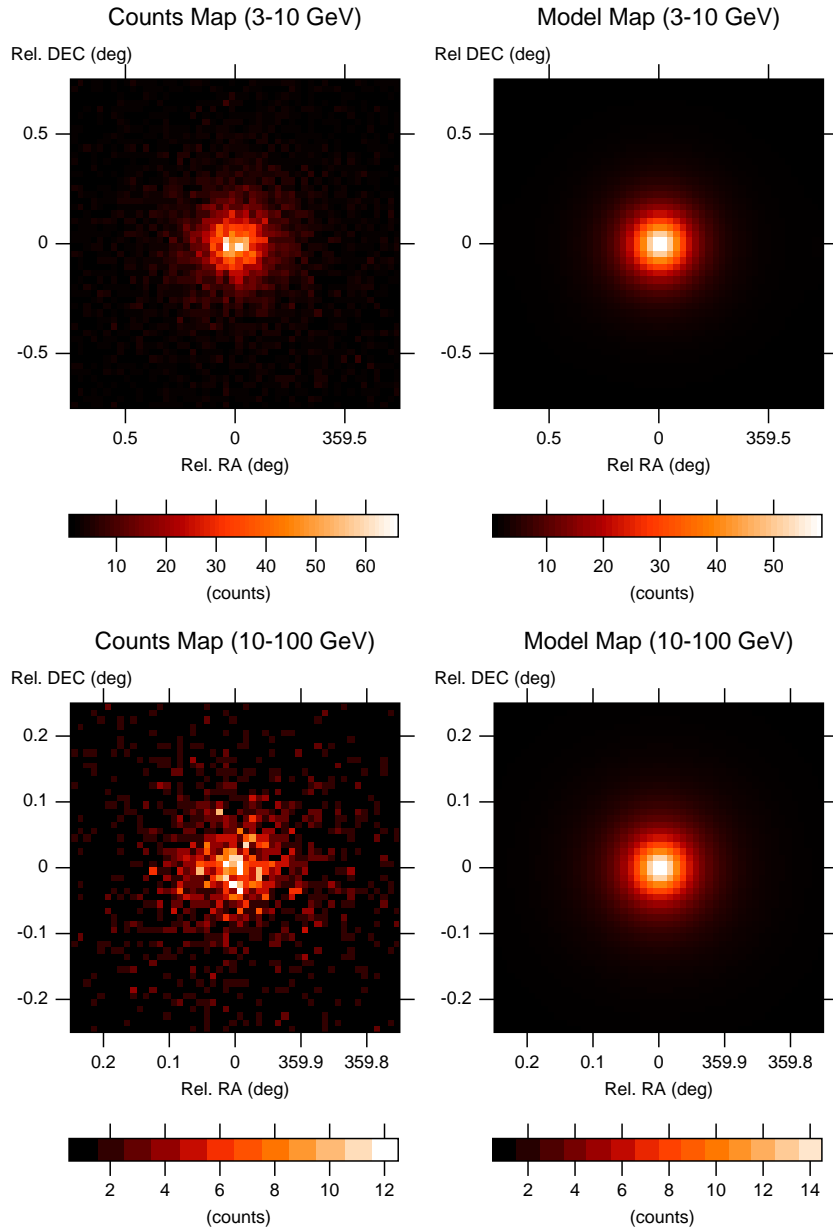


Figure 1: **Gamma-ray counts and point-source model maps of stacked 170 bright AGN.** Upper and lower panels are for 3–10 and 10–100 GeV bands, respectively. Left panels are the actual data counts of stacked 170 AGN, and the right panels show the “best-fit” point-source model. Pixel size is 0.03° (0.01°) for the 3–10 (10–100) GeV band.

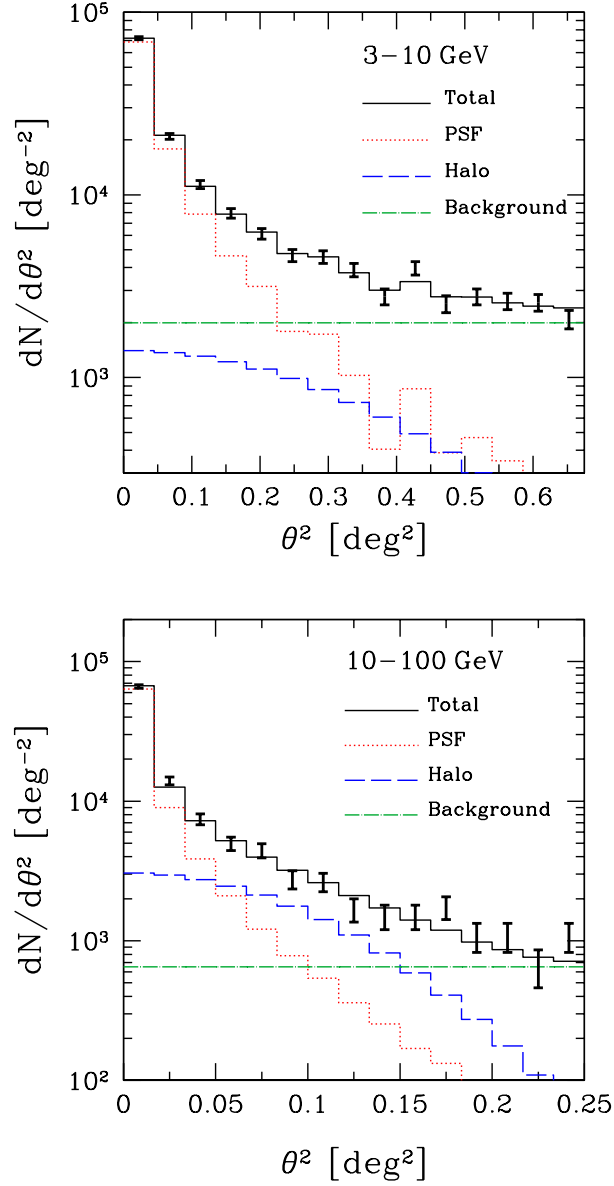


Figure 2: **Surface brightness profile of the stacked gamma-ray images.** Upper and lower panels are for 3–10 GeV and 10–100 GeV bands, respectively. Points with error bars are the data, and solid histogram is the best-fit model. The dotted, dashed, and dot-dashed histograms represent truly point-like source, halo component, and homogeneous diffuse background, respectively.

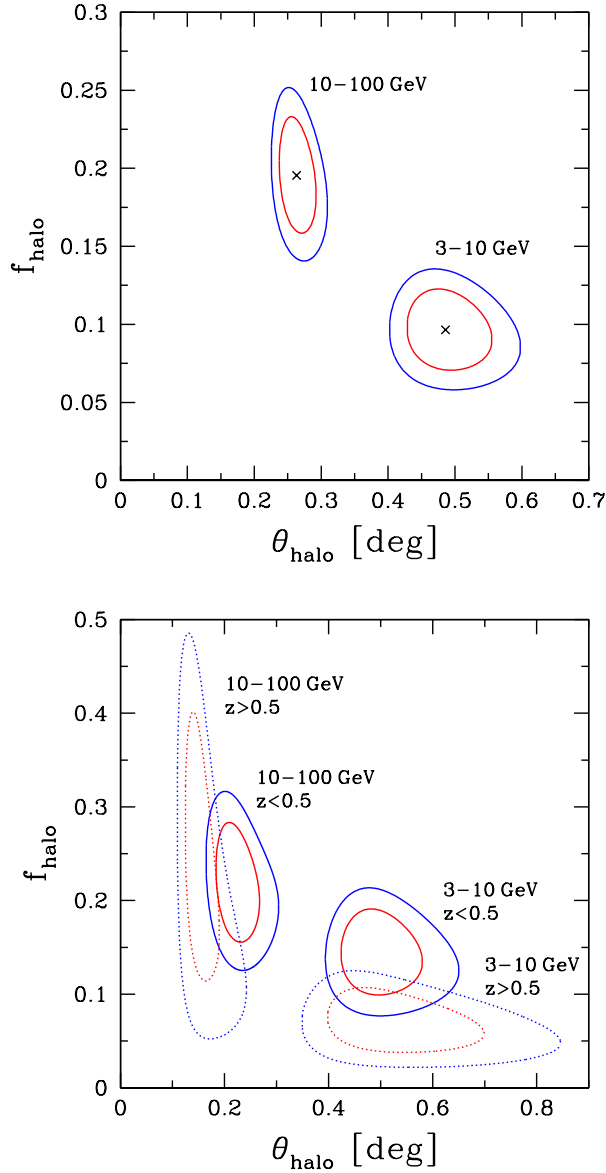


Figure 3: **Allowed regions of halo size θ_{halo} and fraction of events from halo component f_{halo} .** *Top:* Contours are at 68% and 95% confidence level obtained with the sample of 170 AGN. The best-fit values are marked by the crosses. Lower-right and upper-left contours are for 3–10 GeV and 10–100 GeV, respectively. *Bottom:* The same as the top panel but for 99 AGN with known redshifts (again, right and left contours are for 3–10 GeV and 10–100 GeV, respectively). Allowed regions for nearby 57 AGN ($z < 0.5$) are shown by solid contours, and those for distant 42 AGN ($z > 0.5$) are by dotted contours.